J. Fluid Mech. (2004), *vol.* 518, *pp.* 215–229. © 2004 Cambridge University Press
DOI: 10.1017/S0022112004000953 Printed in the United Kingdom

Coherent structures in an oscillatory separated flow: numerical experiments

By PAOLO BLONDEAUX[1], PIETRO SCANDURA[2] AND GIOVANNA VITTORI[1]

[1]Environmental Engineering Department, University of Genova, Via Montallegro 1, 16145 Genoa, Italy

[2]Civil and Environmental Engineering Department, University of Catania, Via A. Doria 6, 95125 Catania, Italy

(Received 16 December 2003 and in revised form 17 June 2004)

Numerical experiments are performed to investigate the oscillatory flow over a two-dimensional wavy wall characterized by a large amplitude, such as to induce flow separation. Even though the Reynolds number is moderate, a three-dimensional turbulent flow is observed. The turbulence dynamics is characterized by the presence of coherent ribs superimposed on the main spanwise vortices generated by the roll-up of the free vortex sheets shed at the crests of the wall waviness. The ribs are formed by the stretching of vorticity patches which are generated by the instability of the two-dimensional flow at two different locations. The first are the saddle points of the flow field created, far from the wall, by the vortex pairs generated every half-cycle. The second are the saddle points created, close to the upstream side of the wavy wall, by the combined action of the free-stream flow and of the vortex structures shed by the ripple crests. Later, the ribs wrap around the main spanwise vortices and cause the distortion of these vortices and the alignement of the vortex lines with the free-stream flow, thus inducing large contributions to the coherent helicity. Simultaneously, regions of high dissipation appear which tend to be separated from those characterized by large values of helicity.

1. Introduction

The numerical simulations of Scandura, Vittori & Blondeaux (2000) have recently shown that, even at moderate values of the Reynolds number, the nominally two-dimensional oscillatory flow over a wavy wall of large amplitude (rippled bed) can contain secondary vortex structures which cause the deformation along the span of the primary large-scale vortices generated by flow separation at the crests of the wall waviness. These secondary structures can be thought to be the result of the instability of the primary two-dimensional oscillatory flow over the wavy wall and to be generated by the development of spanwise perturbations. Hara & Mei (1990) investigating two limiting cases (i.e. weak fluid oscillations over a waviness of finite slope and moderate fluid oscillations over a waviness characterized by very gentle slopes) showed that under suitable conditions, spanwise perturbations of the basic two-dimensional flow can grow and give rise to a three-dimensional flow. To solve the problem by analytical means, Hara & Mei (1990) considered flow parameters such that flow separation is absent and the instantaneous streamlines are always attached to the wavy wall. However, the numerical simulations by Scandura *et al.* (2000)

https://doi.org/10.1017/S0022112004000953 Published online by Cambridge University Press

have shown that the mechanism suggested by Hara & Mei (1990) also operates for separating flows, and spanwise perturbations of the main two-dimensional vortices generated by flow separation can grow and give rise to a complex three-dimensional flow field.

Since coherent vortex structures play a prominent role in the transport of any quantity (mass, momentum, contaminants, etc.), it is worth investigating whether three-dimensional coherent vortices survive to the generating phase and whether they coexist with the main spanwise vortex structures generated by the roll-up of the free shear layers originating at the crests of the wall waviness and with the possible arrays of small-scale vortices created by the break-up of the main vortices. Indeed, in mixing layers the existence of streamwise coherent vortex structures superposed on the main spanwise vortices has been confirmed experimentally (Wygnanski, Oster & Fiedler 1979; Browand & Troutt 1985) even at high Reynolds numbers in a fully developed turbulent flow. On the other hand, there are no experimental data for the case under investigation.

The presence of large-scale spanwise vortices, which interact with each other giving rise to amalgamation and splitting phenomena as well as to the formation of vortex pairs (see e.g. Blondeaux & Vittori 1991, 1999), suggests the existence of saddle points in the flow and therefore the generation of vortex structures known in the literature as ribs (Hussain 1986). In fact, in the analysis of plane mixing layers, wakes and jets, the saddle regions of the flow created by the interaction of spanwise vortices are invariably found to be the location of vortices (ribs) aligned with the diverging separatrix. The continual stretching of the ribs causes them to spin faster due to conservation of angular momentum and counterbalances their decay due to viscous diffusion, which transfers vorticity to the ambient non-vortical fluid. When the vorticity aligned with the diverging separatrix reaches the primary vortex structures with large spanwise vorticity, the ribs are wrapped around the spanwise vortices (rolls) and a strong nonlinear interaction takes place among the different vortex structures. In particular mixing, hence dissipation, occurs at the connection points of the ribs with the rolls. Thus, the locations of dominant vorticity production and dissipation seem to be different. This picture of turbulence dynamics in mixing layers, wakes and jets is supported by flow visualizations and velocity/vorticity measurements as well as by numerical simulations (Hussain 1986). In the present paper, we investigate the topology of the vortices which are present in the oscillatory flow over a wavy wall to see whether the above mechanisms of turbulence production and dissipation are also present in unsteady separated flows. The characteristcs of the wall geometry (amplitude and wavelength of the wall waviness) and those of the fluid oscillations (amplitude and period) have been chosen having in mind the possible application of the results to the study of ripples under sea waves and to the modelling of sediment transport in coastal regions. Indeed, only a full understanding of the dynamics of the coherent vortices generated at the bottom of sea waves can lead to accurate estimates of the apparent bed roughness of the sea bed and to reliable predictions of the sediment transport rates. However, the results obtained are useful to understand turbulence structure in any unsteady separating flow and might be used to formulate new turbulence models.

2. The problem and the numerical approach

As in Scandura *et al.* (2000), we consider the flow of an incompressible viscous fluid of density ρ^* and kinematic viscosity ν^*, above a two-dimensional wavy wall

https://doi.org/10.1017/S0022112004000953 Published online by Cambridge University Press

which is rigid and smooth (hereinafter a star denotes dimensional quantities). Far from the wall, the ambient fluid oscillates harmonically in the direction transverse to the crests of the waviness with velocity $U_0^* \sin(\omega^* t^*)$. As a reference, we define a Cartesian orthogonal coordinate system (x^*, y^*, z^*) with the y^*-axis pointing vertically upwards, and the x^*- and z^*-axes normal and parallel to the ripple crests lying on a horizontal plane coincident with the average bottom. Let us describe the surface profile $y^* = F(x^*)$ parametrically by means of the following relationships (Sleath 1984):

$$y^* = \frac{h^*}{2}\cos(k^*\xi^*), \quad x^* = \xi^* - \frac{h^*}{2}\sin(k^*\xi^*), \tag{2.1}$$

where $k^* = 2\pi/l^*$ is the wavenumber of the waviness, h^* is its height and ξ^* is a dummy variable. The wall surface (2.1) exhibits crests sharper than troughs, like actual ripples under sea waves. The equations governing the fluid motion are written in terms of the orthogonal coordinate system (ξ^*, η^*, χ^*) defined by the following relationships (Sleath 1974):

$$\xi^* = x^* + \frac{h^*}{2}\,\mathrm{e}^{-k^*\eta^*}\sin(k^*\xi^*), \quad \eta^* = y^* - \frac{h}{2}\,\mathrm{e}^{-k^*\eta^*}\cos(k^*\xi^*), \quad \chi^* = z^*, \tag{2.2}$$

which map the wall profile onto the plane $\eta^* = 0$. Moreover, dimensionless variables are introduced using the amplitude U_0^* and the angular frequency ω^* of fluid velocity oscillations far from the bottom to scale the velocity and time respectively, and U_0^*/ω^* as length scale. The dimensionless momentum and continuity equations can be derived following Batchelor (1967, p. 588) and can be found in Scandura *et al.* (2000).

The flow field is determined by numerical means. The governing equations are solved in a rectangular box following a procedure which makes use of second-order finite-difference approximations and is a variant of the fractional step method described in Kim & Moin (1985). Since an integer number of ripple wavelengths is simulated, periodic boundary conditions are forced along the ξ-direction. Periodicity is also forced in the transverse direction χ, which is assumed to be a homogeneous direction. Finally, the no-slip condition is forced at the wall and at the upper face of the computational box a symmetry (stress-free) condition is employed. A stretching of the vertical coordinate is introduced in such a way that the first numerical cell has a height smaller than or equal to $0.1\delta^*$, where δ^* is the viscous length of the phenomenon ($\delta^* = \sqrt{2\nu^*/\omega^*}$). The details of the numerical approach can be found in Scandura *et al.* (2000) where tests made to ascertain the reliability and the accuracy of the numerical code are also described.

3. Results

As already pointed out, the present results have been obtained by fixing the parameters close to the values characterizing actual sea ripples, even though only moderate values of the Reynolds number can be simulated. In particular, two different ripple steepnesses have been considered ($h^*/l^* = 0.125$ and 0.15) and the ratio $(U_0^*/\omega^*)/l^* = 1/l$ between the amplitude of fluid displacement oscillations and ripple wavelength is set equal to 0.75, a value close to that observed in the field (the dimensionless ripple wavelength turns out to be 1.33). Lastly, two different values of the Reynolds number $Re = U_0^{*2}/(\nu^*\omega^*)$ have been considered, namely 1250 and 1600. After a few attempts, the dimensionless width of the computational box in the spanwise direction has been fixed at 2.5, while its length and height have been set

https://doi.org/10.1017/S0022112004000953 Published online by Cambridge University Press

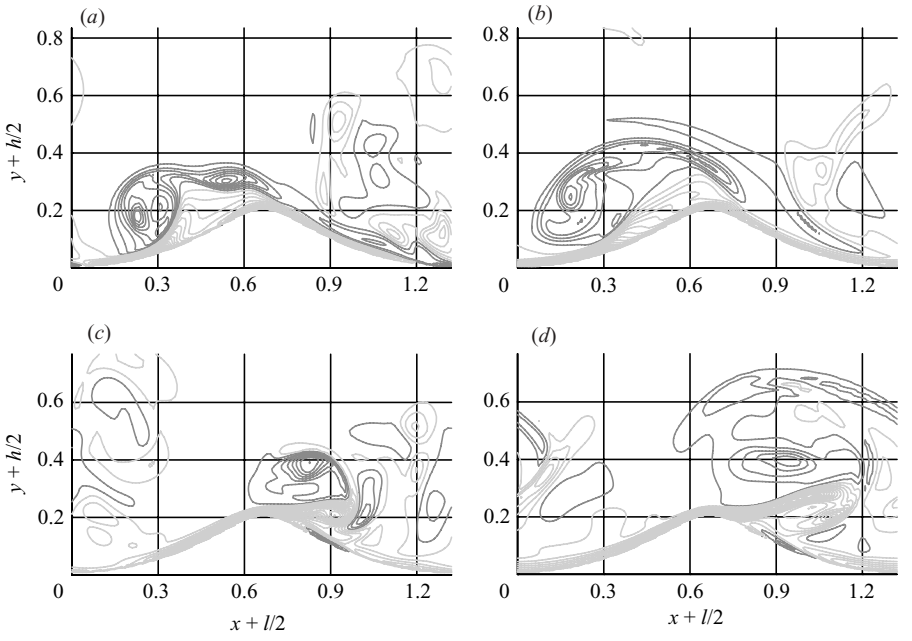


FIGURE 1. Spanwise vorticity component ($\Delta\Omega_z = 4.08$; light grey – negative values; dark grey – positive values). (a,b) $t = 87.96$ $(\phi = 0)$; (c,d) $t = 88.75$ $(\phi = \pi/4)$. (a,c) $z = 1.25$; (b,d) $z = 0.21$ (run 1).

equal to l, i.e. 1.33. The number of grid points in the streamwise, spanwise and vertical directions is fixed at 216, 120 and 216 respectively. As discussed later, this number of grid points ensures that the flow is spatially well resolved. Moreover, during the numerical simulations, the time step Δt changes in such a way that the maximum value of the CFL number is constant, equal to 0.9 which ensure the stability of the numerical approach.

First, the case $h^*/l^* = 0.15$ and $Re = 1600$ (run 1) is discussed. A preliminary analysis of the results has shown that, for these values of the parameters, the flow is characterized by an aperiodic behaviour. However, even though the velocity field does not repeat exactly after a cycle the gross features of the vorticity time development do not differ greatly from one cycle to the next. For this reason, in the following, the flow behaviour is described during a particular cycle (the 15th cycle) when a regime configuration is attained by the flow. In the figure captions both the time t and the phase ϕ within the cycle are given. The gross features of vorticity dynamics do not differ from those described in previous works on the subject and obtained by means of two- and three-dimensional approaches (see e.g. Blondeaux & Vittori 1999; Scandura *et al.* 2000). In figure 1 the spanwise component of vorticity is shown at two different phases of the cycle in the planes $z = 0.21$ and 1.25. Note that in figure 1 and in the following figures the crest of the ripple is located in the middle of the drawing. At $t = 87.96$ $(\phi = 0)$, the fluid is about to reverse its motion. On the left of the figure, one positive (counterclockwise) vortex is present which has been originated by the vorticity shed by the crest during the previous half-cycle. Then, this vortex is no longer fed and is simply convected by the local velocity from the left to the right, interacting with the negative vortex sheet which is shed by the crest of the waviness. In particular, at $t = 88.75$ $(\phi = \pi/4)$, the effects of the free-stream velocity, which is growing, are

https://doi.org/10.1017/S0022112004000953 Published online by Cambridge University Press

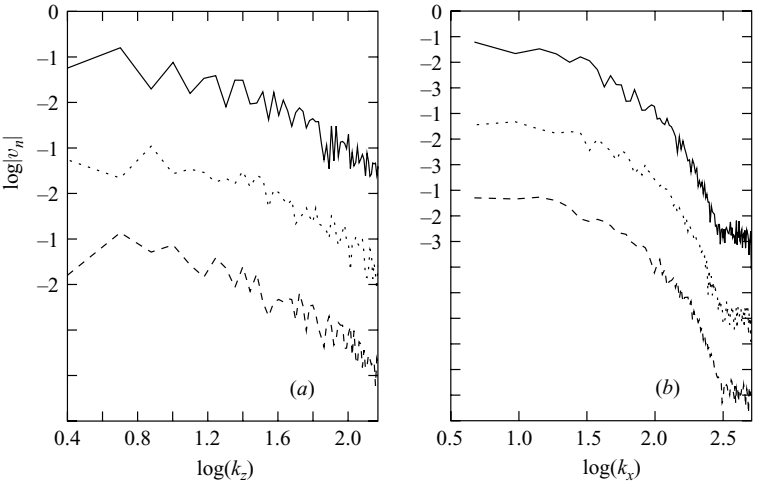


FIGURE 2. Velocity spectra in the spanwise direction for (*a*) $x+l/2=0.86$, $y+h/2=0.43$ and (*b*) in the streamwise direction for $y+h/2=0.43$, $z=1.25$ at $t=88.75\,(\phi=\pi/4)$ (streanwise velocity component, continuous line; vertical velocity component, dotted line; spanwise velocity component, broken line) (run 1).

superposed on those induced by the passage of the positive vortex structure near the crest of the ripple. Therefore, a strong negative vortex sheet is shed at the crest of the ripple and its roll-up gives rise to a negative vortex structure. Then, the positive and negative vortices form a vortex pair which moves because of the free-stream velocity and the self-induced velocity. Later, as shown by figure 3, the vortex pair dissipate because of viscous effects. Simultaneously, further negative vorticity is shed at the ripple crest and a new negative vortex is formed. Similar results can be observed when different vertical planes characterized by different values of z are considered, even though the different locations of the vorticity maxima and minima suggest that the spanwise vortices have a transverse wavy configuration characterized by an amplitude which grows in time (compare figures 1*a*, 1*b*, 1*c* and 1*d*). Even though the vorticity fields are not plotted in figure 1 to save space, during the following half-cycle the gross features of the flow are the mirror images of those previously described.

In figure 2 the spectra of the three velocity components along the z^*- and x^*-directions are shown at a particular phase of the cycle ($t=88.75, \phi=\pi/4$) for $x=0.86$, $y+h/2=0.43$ and $y+h/2=0.43$, $z=1.25$ respectively. The results displayed in figure 2 show that the velocity field is well-resolved in the computational space. Indeed, the highest wavenumber components have a small amount of energy. The spectra are displayed for particular values of the spatial coordinates and of time but are representative of the whole numerical solution.

To make a more exhaustive investigation of the vortex structures which characterize the three-dimensional oscillatory flow over a wavy wall, we identify coherent vortices by means of the procedure suggested by Jeong & Hussain (1995) and later used by Jeong *et al.* (1997). First, we compute the eigenvalues of the symmetric tensor $\boldsymbol{D}^2+\boldsymbol{\Omega}^2$, where $\boldsymbol{D}$ and $\boldsymbol{\Omega}$ denote the symmetric and antisymmetric parts of the velocity gradient tensor respectively. Then, the vortex structures are thought to be localized in the regions characterized by two negative eigenvalues. Indeed, as discussed by Jeong & Hussain (1995), these regions do correlate well with vortex structures buried in the background vorticity. This vortex definition captures the pressure minimum in a

https://doi.org/10.1017/S0022112004000953 Published online by Cambridge University Press

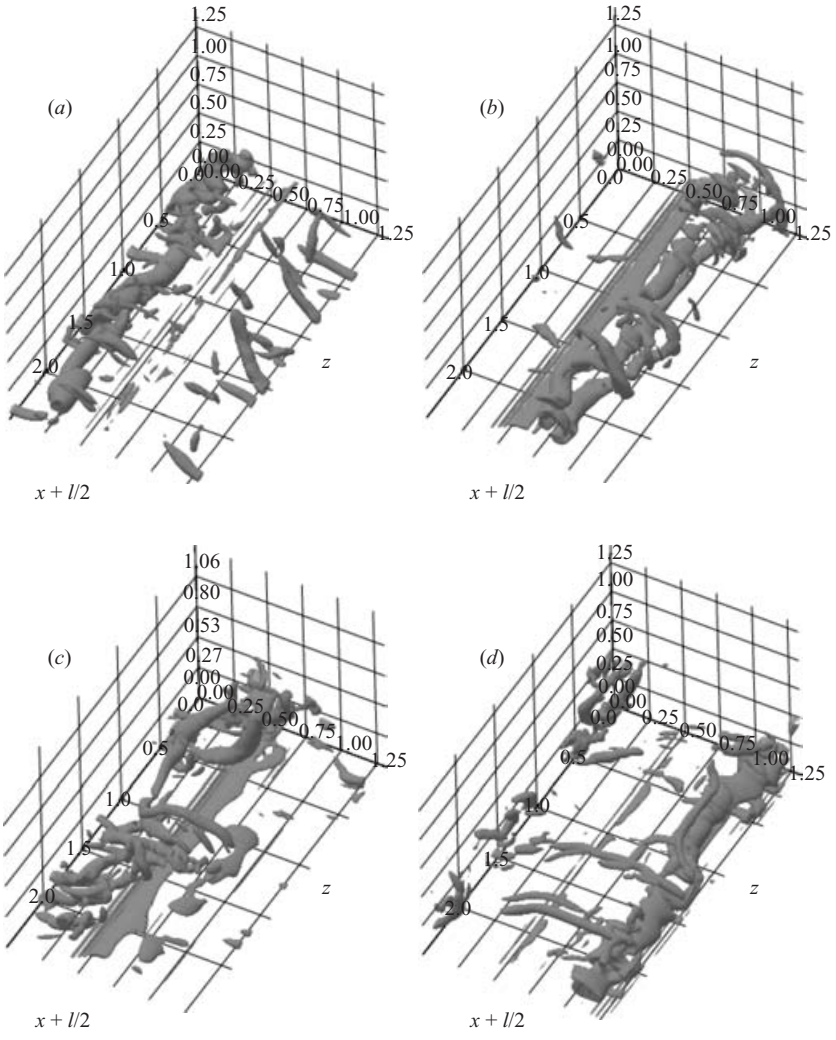


FIGURE 3. Iso-surfaces of λ_2 ($\lambda_2 = -31$) for: (*a*) $t = 87.96$ ($\phi = 0$); (*b*) $t = 88.75$ ($\phi = \pi/4$); (*c*) $t = 89.54$ ($\phi = \pi/2$); (*d*) $t = 90.33$ ($\phi = 3\pi/4$) (run 1).

plane perpendicular to the vortex axis at high Reynolds numbers and also accurately defines vortex cores at low Reynolds numbers.

Figure 3 visualizes iso-surfaces characterized by a negative value of the second eigenvalue (λ_2) of the tensor $\boldsymbol{D}^2+\boldsymbol{\Omega}^2$, at different phases of the cycle. An analysis of the regions where λ_2 is negative confirms the existence of the spanwise vortices displayed in figure 1 but it shows the presence of further vortex structures characterized by coherent dynamics. At $t = 87.96$ ($\phi = 0$), the free-stream flow is about to reverse its motion. A spanwise vortex structure, well above the ripple trough, can be recognized which corresponds to the counterclockwise vortex generated during the previous half-cycle. Moreover, further small vortex structures are present which have been previously generated and are dissipating. Later on, the counterclockwise vortex is convected from the left to the right and clockwise vorticity is shed at the crest of the ripple and gives rise to a negative-λ_2 region adjacent to the ripple crest. Then, the negative vortex sheet rolls up and produces a clockwise vortex structure (see

https://doi.org/10.1017/S0022112004000953 Published online by Cambridge University Press

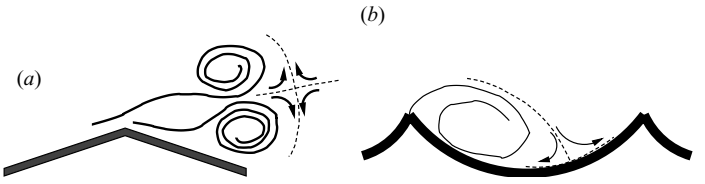


FIGURE 4. Sketch of the saddle regions originated by (*a*) a vortex pair; (*b*) a vortex interacting with the wavy wall.

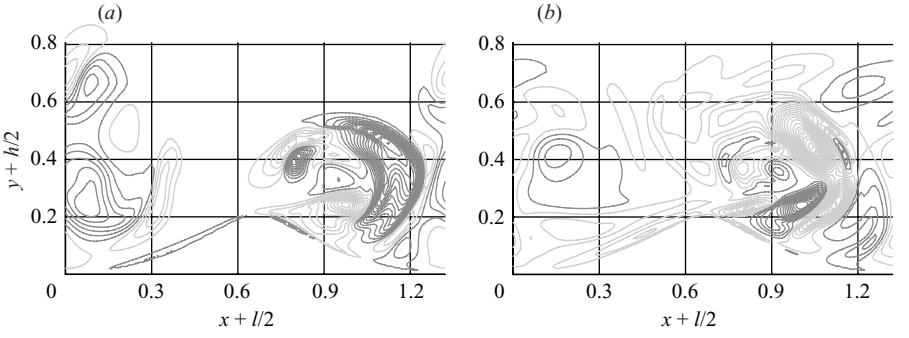


FIGURE 5. Vertical vorticity component ($\Delta\Omega_y = 1.37$; light grey − negative values; dark grey − positive values) at $t = 88.75$ ($\phi = \pi/4$). (*a*) $z = 1.42$, (*b*) $z = 1.92$ (run 1).

the results at $t = 88.75$ ($\phi = \pi/4$)) which strongly interacts with the counterclockwise vortex and gives rise to a vortex pair which creates a saddle point in the velocity field (see the sketch in figure 4*a*). Experimental and numerical studies (for references see Rogers & Moser 1992) suggest that this local flow is unstable with respect to spanwise perturbations, the growth of which gives rise to local vortices with their axis lying in a plane parallel to the (x, y)-plane.

The continual stretching which is present at the saddle point causes any small vortex characterized by vorticity aligned with the diverging separatrix to spin faster due to the conservation of angular momentum. Hence, in the saddle region, vortex structures (ribs) aligned with the diverging separatrix appear (see figure 3*b*). The mechanism of rib generation is similar to that originating rib structures in a plane mixing layer. There has been disagreement as to whether the secondary instability which leads to the formation of rib vortices in the mixing layer and to three-dimensionality is a 'core instability' or a 'braid instability'. Rogers & Moser (1992) found that Pierrehumbert & Widnall's (1982) translative instability eigenfunctions include rib vortices in the braid region and oppositely signed streamwise vorticity in the roller. Since the rib vortices grow with the roller perturbations, the process should be viewed as an instability of the two-dimensional mixing layer as a whole.

Even though there are no theoretical results for the present rapidly changing flow, the similarities of the vorticity topology suggest that the three-dimensionality of the flow and the ribs arise because of the instability of the whole local flow. In figure 3(*b*), four large ribs are evident at z equal to about 0, 0.5, 1.5 and 2.0. Since there is no obvious mechanism through which ribs can introduce net vorticity into the flow, the ribs are expected to alternate in sign, in such a way that their total net vorticity is zero. Figure 5 displays the vertical vorticity component in planes which cross adjacent ribs and shows the different sign of rib rotation. Later on, the ribs are wrapped around the main vortices and the vortex lines are turned and aligned with the free-stream flow

https://doi.org/10.1017/S0022112004000953 Published online by Cambridge University Press

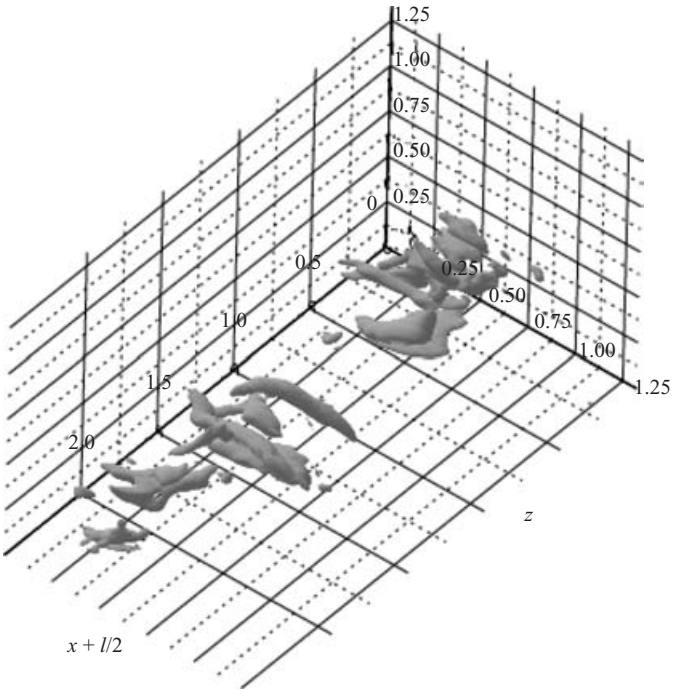


FIGURE 6. Iso-surface of the absolute value of helicity ($|H| = 15$) at $t = 89.54$ ($\phi = \pi/2$) (run 1).

thus causing large contributions to the coherent helicity (compare figure 3*c* which displays negative values of λ_2 at $t = 89.54$ ($\phi = \pi/2$) and figure 6 which shows the absolute value of helicity at the same phase of the cycle).

Around $t = 90.33$ ($\phi = 3\pi/4$), a similar mechanism operates which generates streamwise vortex structures. Indeed, the fluid is strongly accelerated in the positive x-direction along the upstream side of the ripple because the free-stream flow is strong and feels the presence of the wavy wall. Simultaneously, the fluid along the lee side of the ripple moves in the opposite direction because it feels the presence of the vortex structure created by the splitting and roll-up of the clockwise vortex layer shed by the crest. Hence, a saddle point of the flow field is created (see the sketch drawn in figure 4*b*) which gives rise to the growth of spanwise perturbations. Then, the streching of the vortices which are aligned with the diverging separatrix causes them to spin faster due to conservation of angular momentum. Therefore, strong longitudinal vortex structures are generated close to the wavy wall and can by clearly recognized at z equal to about 0.5, 1.5 and 2 (see figure 3*d*). Also, in this case there is no obvious mechanism to introduce net vorticity and the streamwise vortices are expected to alternate in sign, in such a way that their total net vorticity is zero. Indeed, if the streamwise vorticity component is plotted in vertical planes crossing adjacent longitudinal vortices, it clearly appears that it takes the opposite sign (see figure 7). When the free-stream velocity decelerates, these streamwise vortices wrap around the main spanwise clockwise vortex distorting it and generating smaller vortices which then dissipate because of viscous effects. It is worth pointing out that the streamwise vortex structures just described induce vorticity layers of opposite sign along the ripple surface and large wall shear stresses also in the spanwise direction.

https://doi.org/10.1017/S0022112004000953 Published online by Cambridge University Press

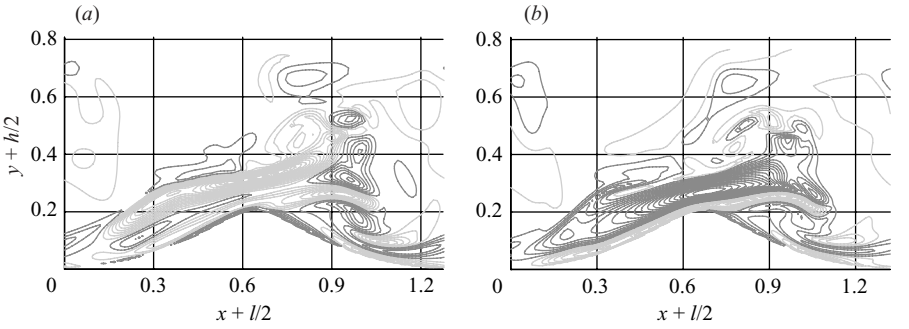


FIGURE 7. Streamwise vorticity component ($\Delta\Omega_x = 2.14$; light grey – negative values; dark grey – positive values) at $t = 90.33$ ($\phi = 3\pi/4$). (*a*) $z = 1.96$, (*b*) $z = 1.92$ (run 1).

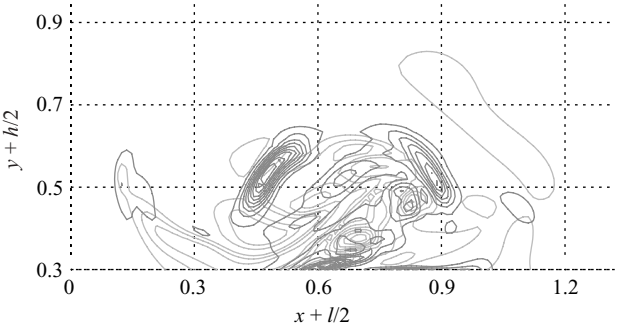


FIGURE 8. Iso-lines of helicity (dark grey, $\Delta H = 2.33$) and dissipation (light grey, $\Delta D = 13.33$) at $t = 89.54$ ($\phi = \pi/2$) and $z = 1.65$. The phase of the cycle has been chosen such that large values of helicity and dissipation are present (run 1).

Thus, it can be guessed that these vortex structures make a significant contribution to sediment motion if ripples under sea waves are considered.

Moffatt (1985) suggested that turbulence at high Reynolds numbers should be characterized by coherent vortex structures which exhibit strong helicity and are separated by layers of high dissipation. In other words, at high Reynolds numbers domains of large helicity and large dissipation are spatially exclusive. As shown by Tsinober & Levich (1983) in an experimental context, coherent structures do indeed frequently exhibit strong helicity (positive or negative). If figure 3(*c*), which shows coherent vortex structures (identified by regions of large negative values of λ_2), is carefully compared with figure 6, which shows regions of high helicity, it can be recognized that in the present numerical simulation coherent vortices also exhibit large values of helicity. The reader should notice that a phase of the cycle is considered such that a highly three-dimensional flow is observed. Moreover, figure 8, where helicity and dissipation are plotted in a region just above the ripple crest where they assume the largest values, shows also that in the present simulation the dissipation term is large where helicity is small and vice-versa. However, because of the moderate value of the Reynolds number, regions of the flow domain where both helicity and dissipation are characterized by large values can be identified.

An attempt to evaluate the rib spacing by computing the auto-correlation of the velocity components in the spanwise direction has been made but no reliable estimate has been obtained. The ribs do form along the diverging separatrix of the saddle

https://doi.org/10.1017/S0022112004000953 Published online by Cambridge University Press

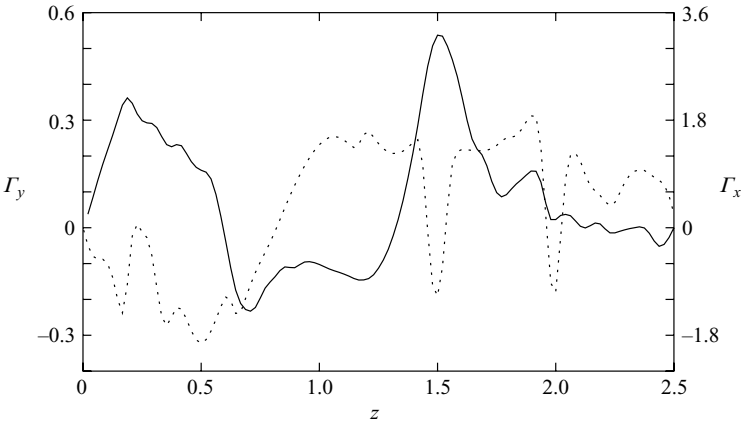


FIGURE 9. Vertical circulation Γ_y (continuous line) for $y+h/2=0.35$, $t=88.75$ ($\phi=\pi/4$) and streamwise circulation Γ_x (dotted line) for $x+l/2=0.67$, $t=90.16$ ($\phi=7\pi/10$) as function of z (run 1).

points of the flow field but at slightly different streamwise locations and different heights from the wall, such as to prevent a reliable estimate of their spacing by means of the auto-correlation evaluated for fixed values of x and y. Hence, an estimate of the rib spacing has been obtained following a procedure similar to that used by Rogers & Moser (1992). The vorticity flux is computed through an horizontal plane extending from $x=0$ to l and from $z=0$ to an arbitrary value

$$\int_0^l \int_0^z \Omega_y \,\mathrm{d}z\,\mathrm{d}x = \int_0^l [u(x,y,z)-u(x,y,0)]\,\mathrm{d}x = \Gamma_y(y,z). \tag{3.1}$$

The use of (3.1) allows an easy evaluation of the vorticity flux. By plotting the vorticity flux, i.e. the vertical circulation Γ_y, as a function of z and counting the relative maxima/minima, the number of positive/negative rotating ribs crossing the horizontal plane can be obtained. In counting the relative maxima/minima, the oscillations characterized by an amplitude smaller than one tenth of the difference between the absolute maximum and minimum values of $\Gamma_y(z)$ have been discarded. This procedure has shown that a reproducible mean spacing exists if y is chosen in such a way that the horizontal plane crosses the ribs. A similar procedure has shown that a reproducible mean spacing of the streamwise vortices generated along the upstream side of the ripple exists too. In the latter case, the vorticity flux through a vertical plane parallel to the ripple crests should be computed along with the streamwise circulation Γ_x. Figure 9 shows the vertical circulation Γ_y and the streamwise circulation Γ_x as function of z, computed for $y+h/2=0.35$, $t=88.75$ ($\phi=\pi/4$) and for $x=0.67$, $t=90.16$ ($\phi\approx 7\pi/10$), respectively. The mean spanwise spacing of the ribs, generated by the vortex pairs, turns out to be about $9\delta^*$ while the mean spanwise spacing of the streamwise vortices, forming along the upstream side of the ripples, is approximately equal to $7\delta^*$. These values can be also estimated by looking at figure 3 and taking into account that the spatial coordinates have been made dimensionless using the quantity U_0^*/ω^* and the ratio $(U_0^*/\omega^*)/\delta^*$ is equal to $\sqrt{Re/2}$.

When the streamwise vortices generated at the wall along the upstream side of the ripple are considered, it is interesting to relate the rib spacing to the thickness of the viscous sublayer. Figure 10 shows the wall shear stress τ averaged in the z-direction at different phases of the cycle as a function of x. At the beginning of the

https://doi.org/10.1017/S0022112004000953 Published online by Cambridge University Press

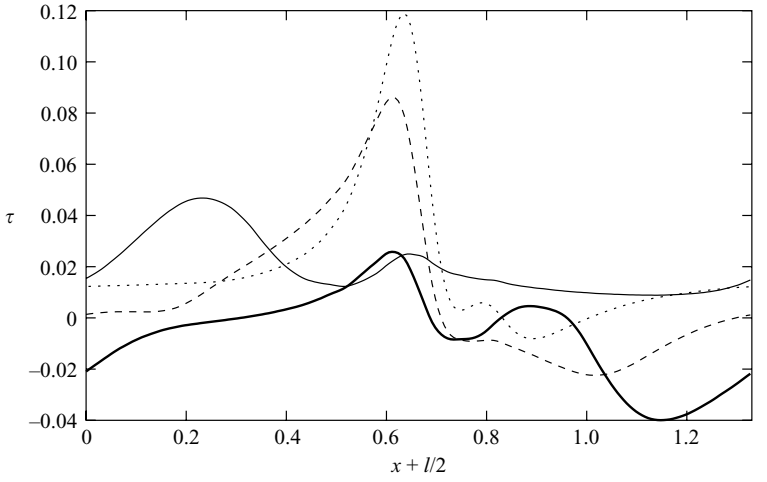


FIGURE 10. Wall shear stress τ as function of x at different phases of the cycle (thinner continuous line, $t = 87.96$ ($\phi = 0.$); dotted line, $t = 88.75$ ($\phi = \pi/4$); broken line, $t = 89.54$ ($\phi = \pi/2$); thicker continuous line, $t = 90.33$ ($\phi = 3\pi/4$) (run 1).

cycle ($t = 87.96$, $\phi = 0$), a large counter-clockwise vortex is present on the left of the ripple crest and it induces large values of the wall shear stress for $0 < x + l/2 < 0.4$. A second smaller relative maximum of the wall shear stress is present at the ripple crest, where the flow accelerates because of the geometrical constraint induced by the wall waviness. At $t = 88.75$ ($\phi = \pi/4$) the counter-clockwise vortex structure has been convected from the left to the right and is located just above the crest, where the wall shear stress attains its maximum. Later on, clockwise vorticity is shed by the ripple crest and a clockwise rotating vortex appears. It follows that negative values of the wall shear stress are generated on the right of the ripple crest. These negative values grow and at $t = 101.10$ ($\phi = \pi$), the wall shear stress distribution is the mirror image of that at $\phi = 0$. The spatial average (along the x-direction) of the absolute value of the dimensionless wall shear stress ($\tau^*/(\rho^* U_0^{*2})$) at $\phi \approx 7\pi/10$ can be computed and is about 0.016. Hence, the ratio between the rib spacing and the viscous length $\nu^*/\overline{u_\tau^*}|_{\phi \approx 7\pi/10}$ is about 50. Taking into account that the slow fluid, which is near the wall, is convected far from it by two counter-rotating ribs, the spacing of the low-speed streaks appearing along the upstream side of the ripple turns out to be about $100\nu^*/\overline{u_\tau^*}|_{\phi \approx 7\pi/10}$, a value which is similar to the spacing of the low-speed streaks observed in steady (Robinson 1991) and unsteady (Costamagna, Vittori & Blondeaux 2003) boundary layers.

Two other simulations have been made to obtain further information on the phenomenon. The first (run 2) is characterized by a different value of the Reynolds number ($Re = 1250$) but it has the same value of h^*/l^* ($h^*/l^* = 0.15$). The second (run 3) is characterized by a smaller value of the ratio between the ripple height and length ($h^*/l^* = 0.125$) but it has the same value of the Reynolds number ($Re = 1600$). In both cases, the qualitative behaviour of the flow is similar to that previously described, even though quantitative differences are present. Figure 11 shows the iso-surfaces characterized by a negative value of λ_2 for $Re = 1250$, $h^*/l^* = 0.15$ and $t = 49.32$ ($\phi = 17\pi/10$), i.e. for run 2. The flow appears less turbulent than that at $Re = 1600$, $h^*/l^* = 0.15$, even though long longitudinal ribs are still clearly visible. Figure 12, where the time development of the dimensionless turbulent kinetic energy

https://doi.org/10.1017/S0022112004000953 Published online by Cambridge University Press

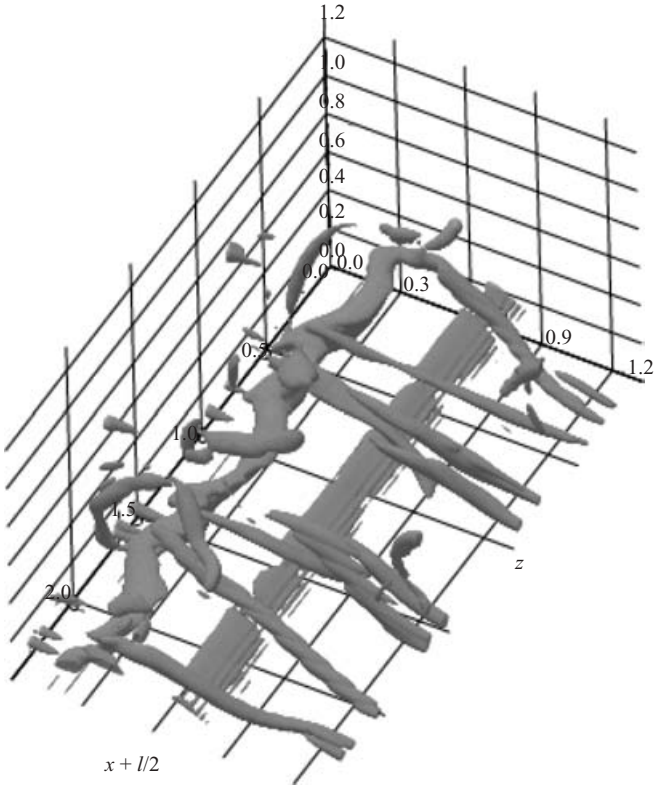


FIGURE 11. Iso-surface of λ_2 ($\lambda_2 = -31$) at $t = 49.32$ ($\phi = 17\pi/10$) (run 2).

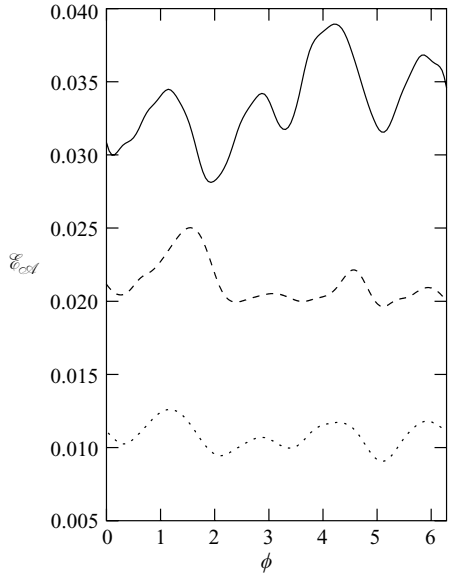


FIGURE 12. Dimensionless turbulent kinetic energy in the computational box per unit area ($\mathscr{E}_{\mathscr{A}}$) as function of the phase within a particular period (continuous line, run 1; broken line, run 2; dotted line, run 3).

https://doi.org/10.1017/S0022112004000953 Published online by Cambridge University Press

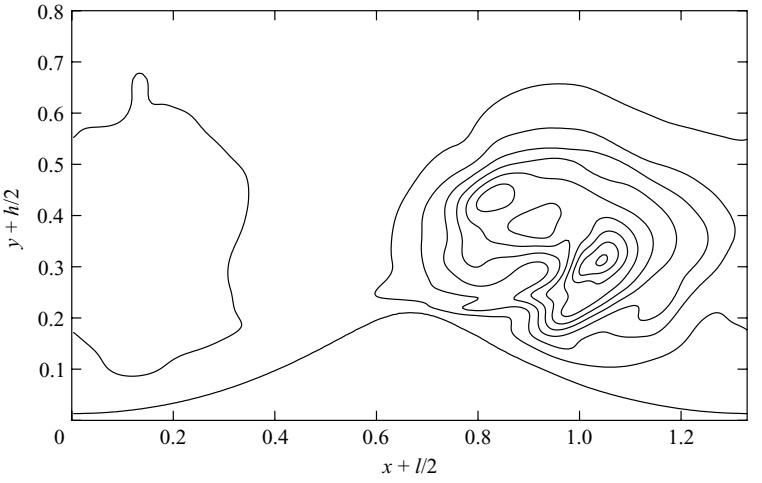


FIGURE 13. Specific turbulent kinetic energy $\mathscr{E}$ averaged in the spanwise direction at $t = 88.75$ ($\phi = \pi/4$) for $Re = 1600$, $h^*/l^* = 0.15$ (run 1).

in the computational box per unit area ($\mathscr{E}_{\mathscr{A}}$) is displayed for the three runs, shows that the case $Re = 1600$, $h^*/l^* = 0.15$ is characterized by the largest values of $\mathscr{E}_{\mathscr{A}}$, while the smallest values are those of run 3. Hence, it appears that not only the Reynolds number but also boundary layer separation and the generation of spanwise vortices play a fundamental role in transition and in turbulence production. Indeed, on decreasing the amplitude of the wall waviness, the vortices generated at ripple crests become weaker till for h^*/l^* smaller than about 0.1 boundary layer separation is absent and no vortex is generated (Sleath 1984). In this case, the flow becomes more stable and turbulence appears only at much higher values of the Reynolds number. This conclusion is supported by the theoretical and experimental works which analyse transition and turbulence structure for a flat bottom (Blondeaux 2001). Moreover, figure 12 shows that turbulence production takes place during time intervals which are slightly different for the three runs but all centred around $t = \pi/4 + n\pi$ and $t \approx 7\pi/10 + n\pi$, i.e. when the ribs are generated and interact with the spanwise rolls. Then, these coherent vortices break and dissipate, thus inducing a rapid decrease of the turbulent kinetic energy. The link between turbulence production and rib generation can also be inferred by looking at figure 13, where the specific turbulent kinetic energy $\mathscr{E} = \frac{1}{2}(\overline{u'^2} + \overline{v'^2} + \overline{w'^2})$ averaged in the spanwise direction is shown at $t = 88.75(\phi = \pi/4)$ as function of x and y for run 1. The largest values of $\mathscr{E}$ are found where the interaction between the ribs and the spanwise rolls takes place. Similar results are found by looking at $\mathscr{E}$ for $t = 90.16$ ($\phi \approx 7\pi/10$). In this case, the maximum values of $\mathscr{E}$ are found along the upstream side of the ripple and where the free shear layer is shed from the bottom profile.

4. Conclusions

Oscillatory flows over a wavy wall (rippled bed), even at moderate values of the Reynolds number, are characterized by a velocity field which experimental measurements (see e.g. Du Toit & Sleath 1981) show to be turbulent. A mechanism which can give rise to an unpredictable velocity field has been pointed out by Vittori & Blondeaux (1991) who have shown that the two-dimensional oscillatory

https://doi.org/10.1017/S0022112004000953 Published online by Cambridge University Press

flow over a rippled bed can become chaotic through an infinite sequence of pitchfork bifurcations (Feigenbaum scenario). However, in actual flows, spanwise perturbations grow and lead to the appearance of a three-dimensional flow, because either centrifugal instability (Hara & Mei 1990) or secondary spanwise instability (Scandura *et al.* 2000) make unstable the basic two-dimensional attached or separated flows respectively. Scandura *et al.* (2000) investigated the nonlinear dynamics of the spanwise perturbations and the early stages of turbulence inception. In the present numerical experiments, the mechanisms of turbulence production and dissipation are elucidated, even though only moderate values of the Reynolds number are considered. Coherent energetic ribs are generated by the stretching of vorticity structures generated by the instability of the basic two-dimensional flow. The stretching takes place along the diverging separatrix of the saddle points created either by pairs of spanwise vortices or close to the upstream side of the wall waviness, because of the simultaneous action of the free-stream velocity and of the vortex shed by the ripple crest. Then, the ribs wrap around the main spanwise vortices and the vortex lines are turned and aligned with the free-stream flow, thus making large contributions to the coherent helicity. Simultaneously, regions of high dissipation appear which tend to be separated by the regions characterized by large helicity. However, because of the moderate value of the Reynolds number of the simulated flow, the regions partially overlap. High computational costs do not allow the investigation of large Reynolds numbers.

REFERENCES

Batchelor, G. K. 1967 *An Introduction to Fluid Dynamics*. Cambridge University Press.

Blondeaux, P. 2001 Mechanics of coastal forms. *Annu. Rev. Fluid Mech.* **33**, 339–370.

Blondeaux, P. & Vittori, G. 1991 Vorticity dynamics in an oscillatory flow over a rippled bed. *J. Fluid Mech.* **226**, 257–289.

Blondeaux, P. & Vittori, G. 1999 Boundary layer and sediment dynamics under sea waves. *Adv. Coast. Ocean Engng* **4**, 133–190.

Browand, F. K. & Troutt, T. R. 1985 The turbulent mixing layer: geometry of large vortices. *J. Fluid Mech.* **158**, 489–509.

Costamagna, P., Vittori, G. & Blondeaux, P. 2003 Coherent structures in oscillatory boundary layers. *J. Fluid Mech.* **474**, 1–33.

Du Toit, C. G. & Sleath, J. F. A. 1981 Velocity measurements close to rippled beds in oscillatory flow. *J. Fluid Mech.* **112**, 71–96.

Hara, T. & Mei, C. C. 1990 Centrifugal instability of an oscillatory flow over periodic ripples. *J. Fluid Mech.* **217**, 1–32.

Hussain, F. 1986 Coherent structures and turbulence. *J Fluid Mech.* **173**, 303–356.

Jeong, J. & Hussain, F. 1995 On the identification of a vortex. *J. Fluid Mech.* **285**, 67–94.

Jeong, J., Hussain, F., Schoppa, W. & Kim, J. 1997 Coherent structures near the wall in a turbulent channel flow. *J. Fluid Mech.* **332**, 185–214.

Kim, J. & Moin, P. 1985 Application of a fractional-step method to incompressible Navier-Stokes equation. *J. Comput. Phys.* **59**, 308–323.

Moffatt, H. K. 1985 Magnetostatic equilibria and analogous Euler flows of arbitrary complex topology. Part 1. Fundamentals *J. Fluid Mech.* **159**, 359–378.

Pierrehumbert, R. T. & Widnall, S. E. 1982 The two- and three-dimensional instabilities of a spatially periodic shear layer *J. Fluid Mech.* **114**, 59–82.

Robinson, S. K. 1991 Coherent motions in the turbulent boundary layer. *Annu. Rev. Fluid Mech.* **23**, 601–639.

Rogers, M. M. & Moser, R. D. 1992 Three-dimensional evolution of a plane mixing layer: the Kelvin-Helmholtz roll-up. *J. Fluid Mech.* **243**, 183–226.

https://doi.org/10.1017/S0022112004000953 Published online by Cambridge University Press

Scandura, P., Vittori, G. & Blondeaux, P. 2000 Three-dimensional oscillatory flow over steep ripples. *J. Fluid Mech.* **412**, 355–378.

Sleath, J. F. A. 1974 A numerical study of the influence of bottom roughness on mass transport by water waves. In *Numerical Methods in Fluid Dynamics* (ed. C. A. Brebbia & J. J. Connor). Pentech Press.

Sleath, J. F. A. 1984 *Sea Bed Mechanics*. Wiley.

Tsinober, A. & Levich, E. 1983 On the helical nature of the three-dimensional coherent structures in turbulent flows. *Phys. Lett.* **99A**, 321–324.

Vittori, G. & Blondeaux, P. 1991 A route to chaos in an oscillatory flow: Feigenbaum scenario. *Phys. Fluids* A **3**, 2492–2495.

Wygnanski, I., Oster, D. & Fiedler, H. 1979 *Turbulent Shear Flows II*. Imperial College.

https://doi.org/10.1017/S0022112004000953 Published online by Cambridge University Press